5Hz GPS seismology of the El Mayor-Cucapah earthquake: Estimating the earthquake focal mechanism

Yong Zheng[1], Jun Li[1,*], Zujun Xie[1], and Michael H. Ritzwoller[2]

1. State Key Laboratory of Geodesy and Earth's Dynamics, Institute of Geodesy and Geophysics, Chinese Academy of Sciences, Wuhan, 430077, China.

2. Center for Imaging the Earth's Interior, Department of Physics, University of Colorado at Boulder, Boulder, CO 80309-0390

Abstract

High-rate (5Hz) GPS records observed in the near-field following the magnitude 7.2 El Mayor-Cucapah earthquake that occurred in northern Mexico on April 4th, 2010 are compared with broad-band seismograms. The high-rate GPS displacement records are consistent with the twice-integrated strong-motion seismic records in the near-field where broadband seismograms are clipped due to strong shaking. Agreement degrades at distances greater than about 150 km from the epicenter where displacement amplitudes approach the noise level of GPS seismograms. Using high-rate GPS data the focal mechanism of the main shock is estimated and is shown to be consistent with teleseismic estimates. The result is seen as confirmation that high-rate GPS observed at near-field stations can be applied together with teleseismic seismometers to yield better information about earthquake rupture properties and parameters.

Keywords: High-rate GPS, strong motion, seismogram, focal mechanism

1. Introduction

The Global Positioning System (GPS) is a constellation of satellites used primarily for navigation purposes to determine position with a precision of about 1 m in real-time. A much higher horizontal precision approaching ~1 mm is achievable via data processing in non-real-time, a fact that has been well exploited to determine long-term deformation in the shallow crust by analyzing changes in position on a daily basis (e.g., Segall and Davis, 1997; Larson et al., 1997, 2004; Wang et al., 2001; and many others). Until recently, the use of GPS instruments for seismological purposes has been the subject of appreciably less work. Interest in this application has been growing, however, because near large earthquakes broad-band seismometers tend to clip and, although strong-motion accelerometers do not, the conversion of acceleration to displacement is degraded by large drifts caused by tilts and the non-linear behavior of the accelerometer (e.g., Trifunac and Todorovska, 2001). For GPS to be used for seismology, much higher sample rates approaching or exceeding 1 sample-per-second are required.

The seismological potential of GPS was first investigated by Hirahara et al. (1994), Ge (1999), Ge et al., (2000), and Bock et al. (2000) who showed that GPS could measure large displacements or instantaneous geodetic positions over very short time spans. Larson et al. (2003) first observed dynamic seismic displacements using GPS following the 2002 magnitude 7.9 Denali Fault (AK) earthquake and demonstrated the similarity between the displacement seismograms determined from GPS and broad-broad seismometers. Bilich et al. (2008) further advanced these investigations. These were largely far-field observations (many hundreds of km) made possible by the strong directivity of the earthquake along the azimuth to distant GPS and seismic instruments. The principal interest in the application of GPS seismology is as a strong motion instrument in the near-field (Larson, 2009). The feasibility of near-field GPS seismology was demonstrated following the 2003 magnitude 6.5 San Simeon (CA) earthquake (Hardebeck et al., 2004; Wang et al., 2007), the 2003 magnitude 8.0 Takachi-Oki earthquake in Japan (Emore et al., 2007), and the 2009 magnitude 6.3 L'Aquila earthquake in Italy (Avallone et al., 2011). GPS seismology has also been shown to be useful in fault rupture inversions alone or in concert with strong-motion and teleseismic data (Ji et al., 2004; Miyazaki et al., 2004; Langbein et al., 2005; Kobayashi et al., 2006; Yokota et al., 2009) and for measuring surface wave dispersion (Davis and Smalley, 2009). Blewitt et al. (2006) demonstrated the effectiveness of GPS to estimate earthquake magnitudes rapidly for tsunami warning and Gomberg et al. (2004) used GPS seismology to study earthquake triggering.

The 4 April, 2010 magnitude 7.2 earthquake (22:40:41.77 GMT), referred to as the El Mayor-Cucapah earthquake, struck Baja California approximately 65 km south of the US-Mexico border (Fig. 1a). This earthquake ruptured along the principal plate boundary between the North American and Pacific plates with a shallow focal depth. Surface rupture of this earthquake extended for about 120km from the northern tip of the Gulf of California northwestward nearly to the international border, with breakage on several faults.

The earthquake occurred where the southern California shear zone, a system of continental parallel right-lateral faults including the San Andreas, San Jacinto and Elsinore faults, connects with a system of transform faults and active spreading centers in the Gulf of California. A high level of historical seismicity has been observed in this region, and this fault system has been active in recent years although the previous large earthquake occurred in 1892 (USGS). The Pacific Plate is believed to move northwestward with respect to the North American Plate at a speed of about 50mm per year. The principal plate boundary in northern Baja California consists of a series of northwest-trending strike-slip faults that are separated by pull-apart basins. The Harvard focal mechanism solution shows that the El Mayor-Cucapah earthquake is a NW-SE dextral lateral strike-slip event, which is consistent with the strike-slip movement of the southeastern part of the Laguna-Salada fault system. However, this earthquake is a rather complex event that may have begun with east-down motion along faults on the eastern edge of the Sierra El Mayor, then ruptured bi-laterally along the Sierra Cucapah fault and the newly detected Indiviso fault, including both transform lateral slip and ridge extension simultaneously (Wei et. al, 2011).

The main shock lasted over 40 seconds (Wei et. al, 2011) and caused strong shaking in the near-field. Based on the USGS survey, the peak ground acceleration (PGA) recorded by strong motion seismometers was as large as 0.59g. Even at epicentral distances greater than 100 km, the PGA was still over 0.1g for some stations (Fig. 1a). For this reason, most of the broadband seismometers close to the epicenter clipped. An example is shown in Figure 1b, which is recorded by station SWS at an epicentral distance of about 100 km.

Because the surface waves of these seismograms are clipped, it is difficult to obtain detailed estimates of the source rupture process using seismic records alone. Thus, other kinds of instruments that are not as seriously affected by strong ground motions are needed to detect the surface displacement. In this work we use high-rate GPS records to obtain near field-ground motions of the El Mayor-Cucapah earthquake and then apply these data to estimate the source mechanism of the main shock.

2. High-rate GPS Data Acquisition and Processing

2.1 Data Acquisition

The Plate Boundary Observatory (PBO) of EarthScope is a geodetic observatory designed to characterize the three-dimensional strain field across the active boundary zone between the Pacific and the western United States. In order to obtain the long period deformation field as well as short-term dynamic motions, two sample rates are used: one sample per second (1 Hz) and five samples per second (5 Hz). At 5 Hz, GPS data can be used to analyze earthquakes at frequencies up to 2.5 Hz. Because the El Mayor-Cucapah Earthquake occurred after construction of the PBO, it was well recorded not only by seismic stations but also by low-rate and high-rate GPS receivers in the US.

In this work, we acquired high-rate GPS data from GPS stations within 250 km of the epicenter (Fig. 1a). Seven stations are located in the region where PGA is higher than 0.22g and around 20 stations are situated where PGA is larger than 0.1g. This distribution provides the opportunity to observe strong ground motion and co-seismic surface displacement of the main shock. We use the high-rate GPS algorithm to solve for the displacements, then correct the displacement record, and finally use the corrected displacements to study the mechanism of the main shock.

2.2 Data processing

There are several differences between the methods for processing the high-rate GPS data and traditional (30 s sampling) GPS data. The most significant difference is related to the technique of eliminating the GPS satellite clock errors and multipath errors. We process the high-rate GPS data similar to the routine method applied in GAMIT software developed at MIT (King and Bock, 2002) which includes the following steps. First, high-rate GPS satellite clock corrections are estimated by using high-rate GPS data obtained from globally distributed receivers with precise satellite orbits and low-rate clocks. In contrast to the satellite clock, the satellite orbit can be safely interpolated onto the satellite's position at any time using a high-degree polynomial (Schenewerk, 2003). Second, we use the track module GAMIT to estimate high-rate receiver coordinates based on high-rate GPS data, the precise satellite orbits, and high-rate satellites clocks from the first step. The reference site should be distant from the main shock and is chosen to be station P553, which is about 440 km from the epicenter. In this study, carrier-phase ambiguities are estimated as float values, the ionosphere-free linear combination (LC) is used to eliminate ionospheric effects, and the tropospheric delays are modeled using a random-walk stochastic process. In the last step, because the high-rate GPS data contains some noise, in order to obtain more accurate solutions, especially for surface displacements caused by earthquakes, the final GPS data requires further filtering. Sideral filtering was suggested by Bock et al. (1991) and was modified by Choi et al. (2004) by considering the satellite repeat time offset to a sidereal day. Further, in this study, a wavelet transform method is also used to de-noise the high-rate GPS results.

2.3 GPS data correction

Although high-rate GPS records are free from clipping, further corrections are needed to obtain reliable ground displacements. Among these corrections, the most important are the removal of linear trends and setting displacement before the arrival of seismic signals to zero (Fig. 2). Figure 2a shows a seismogram with a long period trend. Figure 2b shows an abrupt jump in the record, which is not caused by the earthquake because it occurs before the first arriving seismic phase.

In this study, we use the following methods to remove these disturbances. (1) For the linear trend, the records before the first arriving seismic phase define the pre-arrival background displacement and the signals long after the earthquake signals have passed are taken as the post-arrival background displacement. We then fit linear trends to the pre- and post-arrival background displacement records separately. If the two trends are close to each other, we remove the average fitted trend from the whole seismogram. If the trends are not similar, we remove the pre-arrival and post-arrival trends separately. For the earthquake signal, we extend the trend of the post-arrival part of the record backward in time and then find the trend in the earthquake signal and remove it. (2) For the long period variations of the background displacement, we first find the dominant period band of the variation and then use a wavelet transform method to remove signals in this band. Figure 2c and 2d show the corrected GPS records. Compared with the raw displacement records most disturbances have been removed in the corrected records.

3. Comparison between seismograms and high-rate GPS records

Using the methods described above, time series of horizontal and vertical displacements for 26 high-rate (5-Hz) GPS stations from PBO are obtained. The average error of displacement on the east-west and north-south components is 4.2 mm and 5.4 mm, respectively. However, the error on the vertical component is about 13 mm, more than twice as large as the horizontal components, because atmospheric disturbances cannot be eliminated as well. We analyze the characteristics of the high-rate GPS data here and compare them with seismograms recorded by far-field broadband seismic stations and near-field strong motion seismometers.

Horizontal displacements of representative GPS stations are plotted in Figure 3, where the records are aligned by the origin time of the main event (from SCSN). Hand-picked first arrivals indicate an apparent move-out speed of about 3.4 km/s, which is much slower than the P-wave speed. Because this earthquake initiated weakly (Wei et al., 2011), the P-wave signals apparently are blurred by noise in high-rate GPS records. The first arrivals, therefore, are S-waves in the GPS records. Researchers should be aware that this muting of the P-wave arrivals may affect finite fault inversions.

The dynamic response of the receiver is important to evaluate data quality. In order to check the ability of high-rate GPS records to detect seismic signals, horizontal records from the station P496, which is 62 km from the epicenter, are chosen to analyze the dynamic responses (Fig. 4a). Peak surface displacements at this station are up to 53 cm and 57 cm on the E-W and N-S components, respectively, which are much higher than the noise level. Figure 4b shows the spectrum of the three components at frequencies below 1 Hz. Signal power mainly concentrates between 0.01Hz and 0.3Hz, and decreases rapidly from 0.25Hz to 0.6Hz. This band is appropriate to analyze medium to strong earthquakes. Signal power at frequencies higher than 1 Hz is quite weak and contributes only negligibly to the integrated signal.

In order to quantitatively evaluate the quality of high-rate GPS records, we compare them with records from seismometers. An example is shown in Figure 5a in which the record from GPS station P496 is compared with the displacement integrated from a strong motion accelerograph record (NO. 5058). The two stations are located 61-62 km from epicenter and are separated by less than 1 km, so their displacement seismograms should be similar. We find that the two measurements of displacement are largely consistent. Thus, high-rate GPS measurements can be used to monitor the near-field displacement similarly to strong motion seismometers. On the other hand, the integration of the accelerometer twice to get the displacement tends to amplify biases and distort the true signal. It is, therefore, generally more difficult to correct strong-motion records than GPS records. For these reasons, high-rate GPS records can also be used as a calibration for correcting strong-motion records.

High-rate GPS not only detects strong near-field signals, but also records seismic waves in the far-field, as Larson et al. (2003) demonstrated for the Denali Fault earthquake. Thus, in order to test the characteristics of the far field GPS seismograms, we compare far-field high-rate GPS data with broadband seismograms. An example is shown in Figure 5b. The record from GPS station P472 is compared with the displacement from broadband station 109C; the distance between the two stations is under 100 m but epicentral distance is ~204 km. Here, all seismograms are filtered from 10 sec to 50 sec period. The early arriving body waves are in relatively good agreement with the seismograms, but the GPS records are enriched in low frequencies. However, in the GPS record there is an unexpected signal following the seismic signal between 120 to 200 sec after the main shock, as shown in Figure 5b. This signal is also observed at other GPS sites. This later arrival is an artifact caused by data processing. We use one site as a reference site and the displacement shown in Figure 5b is just the displacement of the target site relative to that at the reference site. Although the reference site is farther away from the epicenter than the GPS site, it also can record the movement of the earthquake, but at a later time. Because of the artifact, the reference site should be chosen as far as practical from the site of interest or it may overlap the real signal. On the other hand, if the reference site is too far away from the target GPS site, the paths of the GPS signals are quite different and thus make it difficult to eliminate the GPS satellite clock errors and multipath errors by the method discussed in section 2.2. We choose the reference site based on the following criterion: The reference site should be near the sites of interest, but the interval between the arrival time of the target signal and the artificial signal should be larger than the length of the wave train of the target signal.

GPS site P553 satisfies this criterion. The GPS waveform in Figure 5b is contaminated by the artifact, but the inversion method is not degraded by it.

4. Focal mechanism inversion with high-rate GPS seismograms

4.1 Methods and data for the focal mechanism inversion

To further validate the high-rate GPS data, we used the data to invert for the focal mechanism of the El Mayor-Cucapah earthquake. Because the noise level of high-rate GPS seismograms is higher than traditional seismometers, we only used GPS stations with epicentral distances less than 150 km in order to improve the signal-to-noise ratio. The Cut and Paste (CAP) method developed by Zhu and Helmberger (1996) and applied subsequently by Zheng et al. (2009) is applied to obtain the focal mechanism. Compared with other focal mechanism inversion methods, such as P-wave first motion polarity and full waveform modeling, the CAP method is more stable and reliable because it separates the whole seismogram into the Pnl wave and the surface waves, which allows them to be shifted independently to fit the synthetic seismograms. This tends to reduce errors caused by the 1D velocity model. The result is, therefore, less sensitive to the velocity model and lateral variations in crustal structure.

Although the CAP method does not require an accurate crustal velocity model, a good velocity model will still improve the inversion accuracy. Because this earthquake has a rupture length of about 120 km, it is hard to find one crustal model to represent the structure between the earthquake and the receivers. For this reason, we use Crust2.0 (Bassin et al., 2000) in the neighborhood of the epicenter as our inversion model, which is sufficiently accurate to provide information about the main shock. The crustal model is listed in Table 1.

4.2 Focal mechanism inversion

Data quality and azimuthal coverage of the stations are important for the inversion for the focal mechanism. Although the CAP method does not require a large number of stations (Tan et al., 2006), relatively better azimuthal station coverage will produce better estimates of focal mechanism and focal depth. Epicentral distance is another factor that is taken into consideration for choosing the stations: the shorter the path, the smaller the degradation caused by uncertainties in the crustal model. Thus, we attempt to choose near-field GPS stations with good data quality as well as to homogenize the azimuthal distribution as much as possible. The selected high-rate GPS stations are shown by red stars in Figure 1. Because all of the stations are located north of the epicenter, the azimuthal coverage is far from homogeneous.

Based on the selected data, a grid search for strike, dip, rake, moment and depth is implemented by the CAP method to obtain the best point-source solution. The search steps for strike, dip and rake angles are all 5 degrees, and the magnitude step is 0.1 magnitude units. By comparing the total misfit from waveform modeling at different depths, we estimated the centroid focal depth to be about 10 km and the best fitting focal mechanism solution is listed in Table 2. The focal mechanisms from the Harvard CMT project, the Southern California Seismic Network (SCSN), and USGS are also presented for comparison (Fig. 6).

The dip and rake angles we observe agree fairly well with the teleseismic estimate from the Harvard CMT, differing only by about 6° and 8°, respectively. There is an apparent discrepancy in the strike angle of about 170°. Figure 7 shows, however, that there are two minima in strike angle, one near 52° and the other near 235°. The 235° strike angle is in better agreement with the orientation of the fault-plane as defined by the aftershock sequence, is about 14° off from the Harvard CMT, and the focal mechanism is in visually better agreement with the seismic studies as Figure 6 illustrates. With this choice of strike angle, however, the dip angle changes to about 103°. Thus, the largest difference in our focal mechanism and the teleseismic mechanisms actually is in the dip angle, where our result differs from the Harvard CMT by about 20°. As Figure 7 illustrates, the dip angle is difficult to observe using near-field data alone under the assumption of an instantaneous point source for such a large earthquake. For dip angles between 50° to 80°, there is little change in misfit. This is why the dip angle of the mainshock in this work is substantially different from the other studies.

From the comparison between observed and synthetic waveforms (Figure 8) we see that although not all of the time segments are fit equally well, most of the cross-correlation coefficients between the synthetics and the observations are larger than 75% and some are even larger than 90%. This level of misfit indicates that the focal mechanism inversion is acceptable.

Remaining discrepancies between the focal mechanisms of USGS, Harvard and this work may be due to several causes. First, the noise level of the high-rate GPS records is higher than that of seismometers, which adds to the ambiguity of the angles of the focal mechanism. Second, the observing network we use is very near the earthquake and subtends a narrow range of azimuths. The proximity of the earthquake to the network degrades the assumption that the earthquake is a point source with an instantaneous rupture. In addition, because nearly all of the stations are north of the US-Mexico border, the azimuthal coverage is highly restricted. The geometry of the focal mechanism is, therefore, difficult to resolve. The general similarity between the focal mechanism obtained from near-field high-rate GPS seismology and teleseismic studies, however, suggests that the GPS observations can be added to teleseismic data for joint analysis.

5. Conclusions and Discussion

We study high-rate GPS records following the El Mayor-Cucapah earthquake within 250 km of the epicenter. These data provide important surface-wave records in the near-field where broad-band seismometers either were clipped or were simply not present. Due to complications in the noise recorded on high-rate GPS, signal de-noising techniques that include linear trend removal and wavelet transformation are developed and applied in this study.

We compare integrated seismometer records (including broadband seismometers and strong-motion accelerometers in the near-field) to the high-rate GPS displacement records. These records are in good agreement for the surface waves in the near-field, but beyond about 150 km the high-rate GPS degrades due to high noise levels believed to be ionospheric in origin.

Combining high-rate GPS in the near-field with seismometers at teleseismic distances may lead to more accurate modeling and imaging of the earthquake rupture sequence and source parameters. To test this hypothesis, based on the corrected high-rate GPS records, the focal mechanism of the El Mayor-Cucapah earthquake is inverted using the CAP method. The method reveals a right-lateral strike-slip mechanism with a shallow focal depth of about 10 km. This result is generally consistent with the solutions from the Harvard CMT project, the USGS, and the SCSN except for a significant difference in the dip angle. Considering the high noise level of high-rate GPS data, the complexity of the rupture process, and the significantly sub-optimal azimuthal coverage of the stations (Fig. 1), the result is seen as confirmation that high-rate GPS observed at near-field stations can be applied in concert with teleseismic seismometers to yield better information about the earthquake rupture properties and parameters. It is, however, strictly not suitable to describe an earthquake as large as the El Mayor-Cucapah earthquake as an instantaneous point source in the near-field. Thus, focal mechanisms based on near-field high-rate GPS either alone or in concert with teleseismic data may be best applied to study small to moderate sized earthquakes.

Acknowledgements:

We acknowledge EarthScope and its sponsor, the National Science Foundation, for providing the data used in this study. This work was supported by CAS grant kzcx2-yw-142, and NSFC grant (40974034, 41174086).

References:

Avallone, A., M. Marzario, et al. (2011). Very high rate (10 Hz) GPS seismology for moderate-magnitude earthquakes: The case of the Mw 6.3 L'Aquila (central Italy) event, *J. Geophys. Res.,* 116, B02305.

Bassin, C., Laske, G., and Masters, G. *(2000).* The current limits of resolution for surface wave tomography in North America*, Eos Trans. AGU 81***,** *Fall Meet. Suppl., F897.*

Bilich, A., J. Cassidy, and K.M. Larson (2008). GPS seismology: application to the 2002 Mw =7.9 Denali Fault earthquake. *Bull. Seism. Soc. Am.,* 98(2), 593-606.

Blewitt, G., C. Kreemer, W.C. Hammond, H.-P. Plag, S. Stein, and E. Okal (2006). Rapid determination of earthquake magnitude using GPS for tsunami warning systems, *Geophys. Res. Lett.,* 33, L11309.

Bock, Y., R. M. Nikolaidis, P.J. de Jonge, and M. Bevis (2000). Instantaneous geodetic positioning at medium distances with Global Positioning System, *J. Geophys. Res*., 105(B12), 28,223-28,253.

Choi, K., A. Bilich, K. M. Larson, and P. Axelrad (2004). Modified sidereal filtering: Implications for high-rate GPS positioning. *Geophys. Res. Lett.*, 31, L22608, doi:10.1029/2004GL021621.

Davis, J.P. and R. Smalley Jr (2009). Love wave dispersion in central North America determined using absolute displacement seismograms from high-rate GPS. *J. Geophys. Res.*, 114, B11303.

Elosegui, P., J. L. Davis, D. Oberlander, R. Baena, and G. Ekstro¨m (2006). Accuracy of high-rate GPS for seismology. *Geophys. Res. Lett.,* 33, L11308, doi:10.1029/2006GL026065.

Emore, G.L., J.S. Hasse, K. Choi, K.M. Larson, and A. Yamagiwa (2007). Recovering seismic displacements through combined use of 1-Hz GPS and strong-motion accelerometers, *Bull. Seism. Soc. Am.,* 97(2), 357-378.

Ge, L. (1999). GPS seismometer and its signal extraction. *in 12th International Technical Meeting of the Satellite Division of the Institute of Navigation*, pp. 41– 52, Inst. of Navig., Fairfax, Va.

Ge, L., S. Han, C. Rizos, Y. Ishikawa, M. Hoshiba, Y. Yoshida, M. Izawa, N. Hashimoto, and S. Himori (2000). GPS Seismometers with up to 20 Hz Sampling Rate. *Earth Planets Space,* 52(10), 881–884.

Gomberg, J., P. Bodin, K. Larson, H. Dragert (2004). Earthquakes nucleated by transient deformations – a fundamental process evident in observations surrounding the M7.9 Denali Fault earthquake. *Nature*, 427, 621-624.

Hirahara, K. et al. (1994). An experiment for GPS strain seismometer. In: *Japanese Symposium on GPS*, 15-16 December, Tokyo, Japan, 67-75.

Ji, C., K. M. Larson, Y. Tan, K. W. Hudnut, and K. Choi (2004). Slip history of the 2003 San Simeon earthquake constrained by combining 1-Hz GPS, strong motion, and teleseismic data. *Geophys. Res. Lett.,* 31,L17608, doi:10.1029/2004GL020448.

King, R.W. and Y. Bock (2002). Documentation for the GAMIT GPS Analysis Software [M], America: Mass Inst. of Technol., Cambridge, Mass.

Kouba, J. (2003a). Measuring seismic waves induced by large earthquakes with GPS. *Stud. Geophys. Geod.,* 47, 741–755.

Kobayashi, R., S. Miyazaki, and K. Koketsu (2006). Source processes of the 2005 West Off Fukuoka Prefecture earthquake and its largest aftershock inferred from strong motion and 1-Hz GPS data, *Earth Planets Space,* 58: 57–62.

Kouba, J. (2003b). A Guide to using International GPS Service (IGS) products, ftp://igscb.jpl.nasa.gov/igscb/resource/pubs/GuidetoUsingIGSProdcts.pdf

Langbein, J., R. Borcherdt, D. Greger, et al. (2005) Preliminary report on the 28 September 2004, M 6.0 Parkfield, California earthquake, *Seism. Res. Lett.,* 76(1):10-26.

Larson, K.M. (2009). GPS seismology, *J. Geod*., 83, 227-233.

Larson, K.M., J.T. Freymueller, and S. Philipsen (1997). Global plate velocities from the Global Positioning System, *J. Geophys. Res.,* 102(B5), 9961-9981.

Larson, K. M., P. Boden, and J. Gomberg (2003). Using 1-Hz GPS data to measure deformations caused by the Denali fault earthquake. *Science,* 300, 1421– 1424.

Larson, K.M., A.R. Lowry, V. Kostoglodov, W. Hutton, O. Sanchez, K. Hudnut, and G. Suarez (2004). Crustal deformation measurements in Guerrero, Mexico. *J. Geophys. Res.,* 109, B04409.

Lichten, S. M., and J. S. Border (1987). Strategies for high-precision Global Positioning System orbit determination. *J. Geophys. Res.,* 92, 12,751–12,762.

Mattia, M., M. Rossi, F. Guglielmino, M. Aloisi, and Y. Bock (2004). The shallow plumbing system of Stromboli Island as imaged from 1 Hz instantaneous GPS positions. *Geophys. Res. Lett.,* 31, L24610,doi:10.1029/2004GL021281.

Miyazaki, S., K. M. Larson, K. Choi, K. Hikima, K. Koketsu, P. Bodin, J. Haase, G. Emore, and A. Yamagiwa (2004). Modeling the rupture process of the 2003 September 25 Tokachi-Oki (Hokkaido) earthquake using 1-Hz GPS data. *Geophys. Res. Lett.,* 31, L21603, doi:10.1029/ 2004GL021457.

Segall, P. and J.L. Davis (1997). GPS applications for geodynamics and earthquake studies. *Annu. Rev. Earth Planet*. Sci.1997. 25:301~336

Schenewerk, M. (2003). A brief review of basic GPS orbit interpolation strategies. *GPS Solutions*, 6, 265-267, doi: 10.1007/s10291-002-0036-0.

Tan, Y., L.P. Zhu, D.V. Helmberger, and C.K. Saikia (2006). Locating and modeling regional earthquakes with two stations, *J. Geophys. Res.,*111, B01306, doi:10.1029/2005JB003775.

Trifunac, M.D. and M.I. Todorovska (2001). A note on the usable dynamic range of accelerographs recording translation. *Soil Dyn. Earthquake Eng.,* 21, 275-286.

Zhu, L.P. and D.V. Helmberger (1996). Advancement in source estimation techniques using broadband regional seismograms. *Bull. Seism. Soc. Am.*, 86(5):1634-1641.

Zheng, Y., H.S. Ma, J. Lv, et al. (2009). Source mechanism of strong aftershocks (Ms≥5.6) of the 2008/05/12 Wenchuan earthquake and the implication for seimotectonics. Sci. China Ser. D-Earth Sci, 52(6), 739-753, doi:10.1007/s11430-009-0074-3.

Wang Q., Zhang P.Z., Freymueller J.T., Bilham R., et al. (2001). Present-day deformation in

China constrained by Global Positioning System measurements. *Science,* 294:574-577.

Wang, G.-Q., D.M. Boore, G. Tang, and X. Zhou (2007). Comparisons of ground motions from colocated and closely spaced one-sample-per-second Global Positioning System and accelerograph recordings of the 2003 M 6.5 San Simeon, California, earthquake in the Parkfield region, *Bull. Seismol. Soc. Am.*, 97(1B), 76-90.

Wei, S., E. Fielding, S. Leprince, et al. (2011), Superficial simplicity of the 2010 Mw 7.2 El Mayor-Cucapah earthquake of Baja California in Mexico, *Nature Geoscience*, 4, 615-618..

Yokota, Y., K. Koketsu, K. Hikima, and S. Miyazaki (2009). Ability of 1-Hz GPS data to infer the source process of a medium-sized earthquake: The case of the 2008 Iwate-Miyagi Nairiku, Japan, earthquake. *Geophys. Res. Lett.*, 36, L12301.

Table 1. The crustal model used in inversion for the focal mechanism. Vp and Vs are P wave velocity and S wave velocity, respectively. Qa and Qb are the Q value of P and S waves.

Thickness (km)	Density (kg/m^3)	Vp (km/s)	Vs (km/s)	Qa	Qb
1.0	2100	2.5	1.2	400	200
0.5	2500	4.4	2.5	600	400
9.0	2750	6.1	3.5	1000	600
8.5	2800	6.3	3.6	800	500

8.5	2900	6.6	3.6	900	400
------	3300	8.0	4.6	972	600

Table 2. The focal mechanism estimated by using near-field high-rate GPS stations compared with solutions obtained by the Harvard CMT, USGS, and SCSN using teleseismic data.

	Mw	Centriod Depth (km)	Strike1	Dip1	Rake1	Strike2	Dip2	Rake2
This work	7.2	10	52	77	-14	146	76	-167
Harvard	7.2	12	221	83	-6	312	84	-173
USGS	7.2	10	222	47	-10	319	82	-135
SCSN	7.2	10	219	84	-17	311	73	-174

Figure captions:

Figure 1. (a) Location of the El Mayor-Cucapah earthquake and the distribution of selected GPS stations. Triangles represent the GPS stations: hollow triangles are the stations > 200 km from the epicenter while the solid triangles are the stations closer than 200 km. The “beachball” is the Harvard-CMT focal mechanism of the main shock located at the epicenter. Gray circles are aftershocks with magnitudes larger than M4.0. The red stars are locations of

the high-rate GPS stations used in the inversion for the focal mechanism, and the largest red star is the epicenter of the mainshock. The red square and red diamond are the locations of the broadband seismic station and the strong motion seismic station of Fig. 5. The white contour lines show strong motion of the earthquake, with units in percent of gravitational acceleration, g. The inset enlarges the area outlined by the black rectangle. (b) Clipped broadband seismograms following the El Mayor-Cucapah earthquake recorded at the broadband seismograph at station SWS, located about 100 km from the epicenter.

Figure 2. Correction of high-rate GPS data. (a) North-South component GPS record showing a linear trend (GPS site P507, approximately 109 km from the epicenter). (b) North-South component GPS record illustrating signals arriving before the seismic waves (GPS site P511, approximately 181 km from the epicenter). (c) GPS record corrected by removing a linear trend (GPS site P507). (d) GPS record corrected by removing the background signals (GPS site P511). All records are bandpass-filtered from 3.3 to 100 sec period.

Figure 3. East-West and North-South components of the ground displacements observed with the 5-Hz GPS data. The stations are ordered by epicentral distance. The thick black lines show a move-out with speed of ~3.4km/s.

Figure 4. Displacements and spectral amplitudes of GPS records at site P496,

approximately 62 km from the epicenter. (a) Displacements on E-W, N-S and vertical components. (b) Spectral amplitude distribution of the high-rate GPS records.

Figure 5. Comparisons of the seismic waves observed on seismometers with the high-rate GPS records. (a) Comparison of 5HZ GPS displacement record at station P496 (62 km from the epicenter) and the displacement record obtained by twice integrating data from the strong motion accelerograph station 5058 (61 km from the epicenter). The distance between GPS station P496 and strong motion station 5058 is less than 1km, the GPS signal has been bandpass filtered from 50 sec to 0.2 sec period. (b) Comparison of the 5HZ GPS displacement record at station P472 and the displacement records at broadband station 109C, which belongs to USArray and was obtained by integrating velocity to displacement. The distance between the receiver and the epicenter of the El Mayor-Cucapah earthquake is 204 km, and the distance between GPS station P472 and seismic station 109C is negligible. The reference zero time is the time of the mainshock.

Figure 6. Visual comparison of the focal mechanisms determined here with the Harvard CMT, USGS and SCSN. Two of our focal mechanisms are shown, one with strike angle of 52° (far left) and the other with strike angle of 235° (far right).

Figure 7. The variation of misfit error with rake, dip and strike angles, from top to bottom,

respectively. For misfit as a function of each source parameter, the other two parameters are set to our values presented in Table 2.

Figure 8. Comparison between the observed and synthetic seismograms of the El Mayor-Cucapah earthquake. The red lines are the synthetic seismograms and the black lines are the observed high-rate GPS displacement waveforms. The frequency band of Pnl waveforms are 0.05-0.2Hz while for surface waves it is 0.05-0.10Hz. The top line gives the fit and one fault plane of the earthquake and the beachball shows the focal mechanism of the earthquake. The small circles on the beachball are the P-locations of the stations in which a lower hemisphere projection is used to draw the beachball. The first column gives the azimuth, name and distance to the station. The other 5 columns are used to compare the synthetic and observed seismograms, from left to right the phases are: vertical component of Pnl (Pnl V), radial component of Pnl (Pnl R), vertical component of surface wave, radial surface wave component, and SH wave (Tang.). The synthetic waveform and the observed seismogram are aligned by cross-correlation, the two numbers under the corresponding components are the time shift between the two waveforms and the cross-correlation coefficient between the two waveforms. Detailed information about the method can be found in the article about CAP method (Zhu and Helmberger, 1996).

(a)

(b)

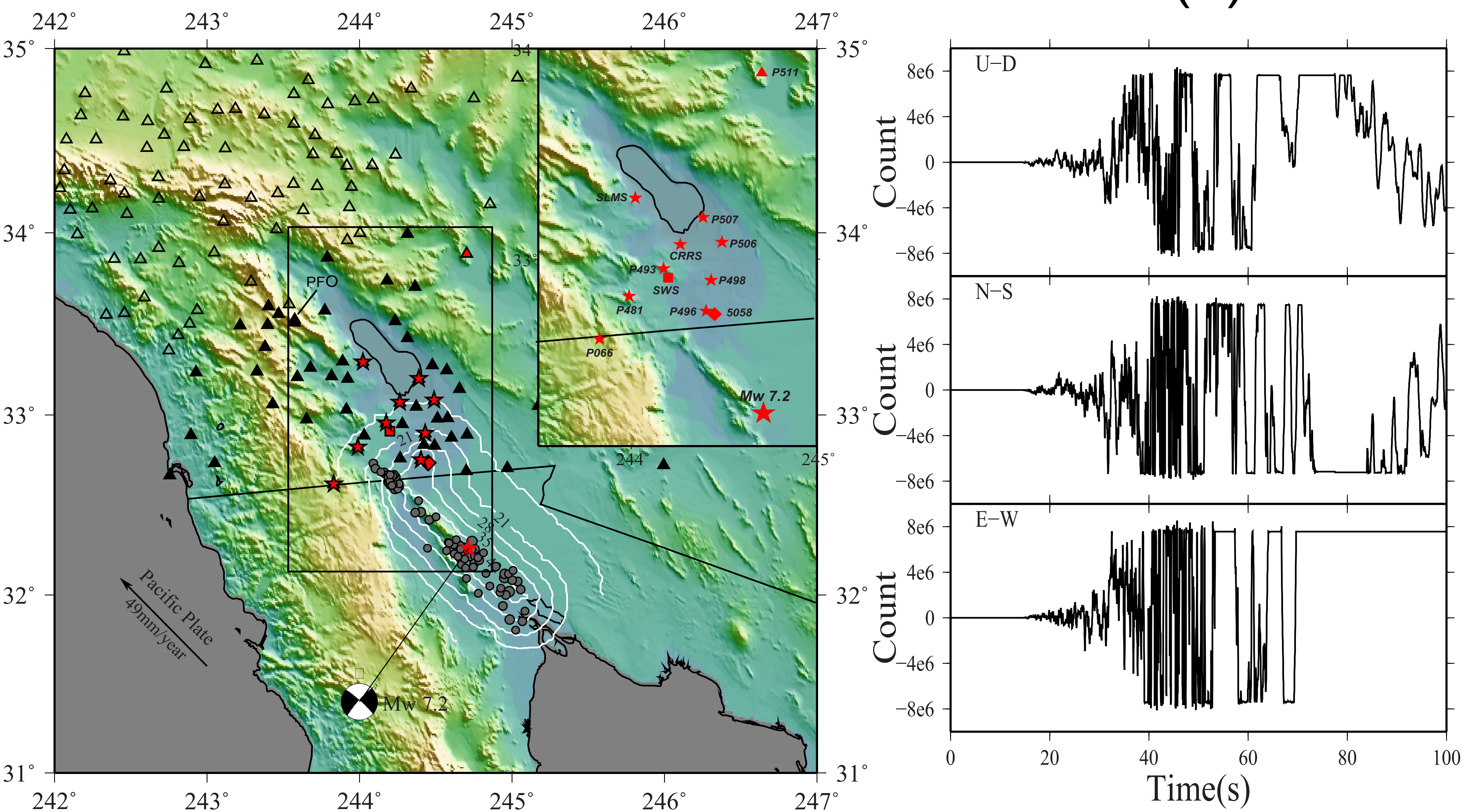

242° 243° 244° 245° 246° 247°
35° 34° 33° 32° 31°
PFO
Pacific Plate
49mm/year
Mw 7.2
P511
SLMS
P507
P506
CRRS
P493
P498
SWS
P481
P496
5058
P066
Mw 7.2
U-D
N-S
E-W
Count
8e6
4e6
0
-4e6
-8e6
0 20 40 60 80 100
Time(s)

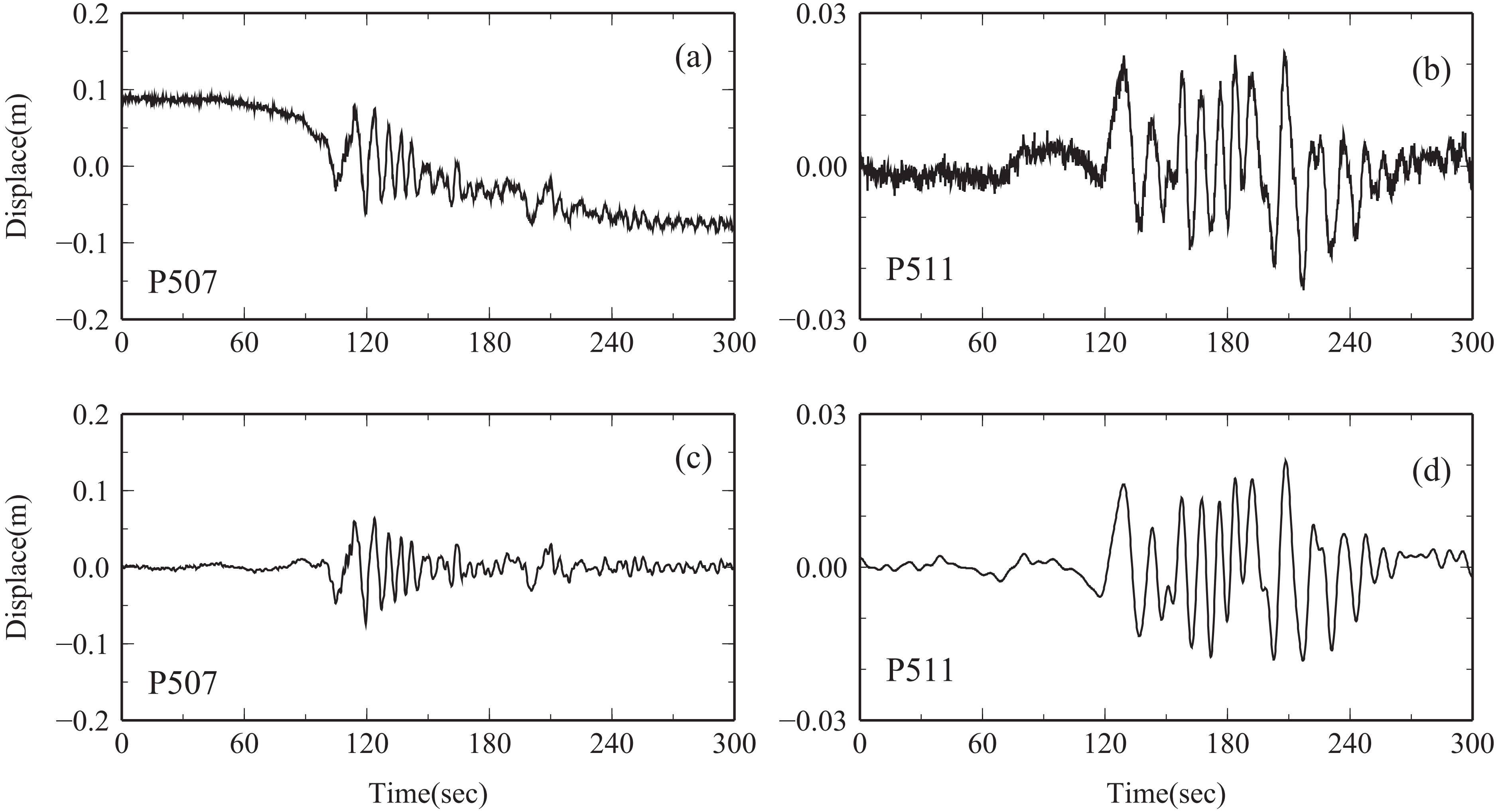

(a)
(b)
(c)
(d)
P507
P511
P507
P511
Displace(m)
Displace(m)
Time(sec)
Time(sec)
0.2
0.1
0.0
−0.1
−0.2
0.03
0.00
−0.03
0
60
120
180
240
300

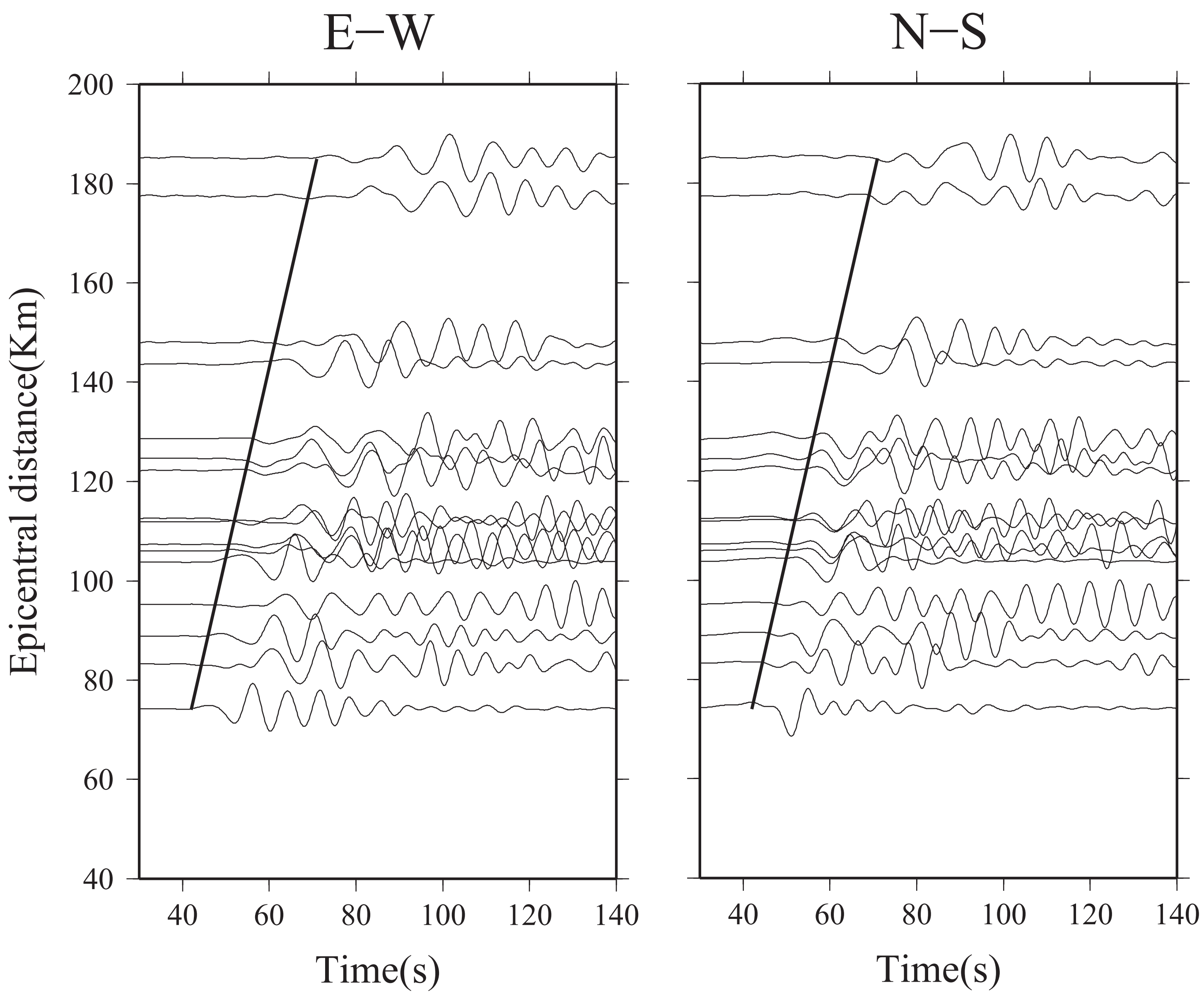

E−W
N−S
Epicentral distance(Km)
200
180
160
140
120
100
80
60
40
40 60 80 100 120 140
Time(s)
40 60 80 100 120 140
Time(s)

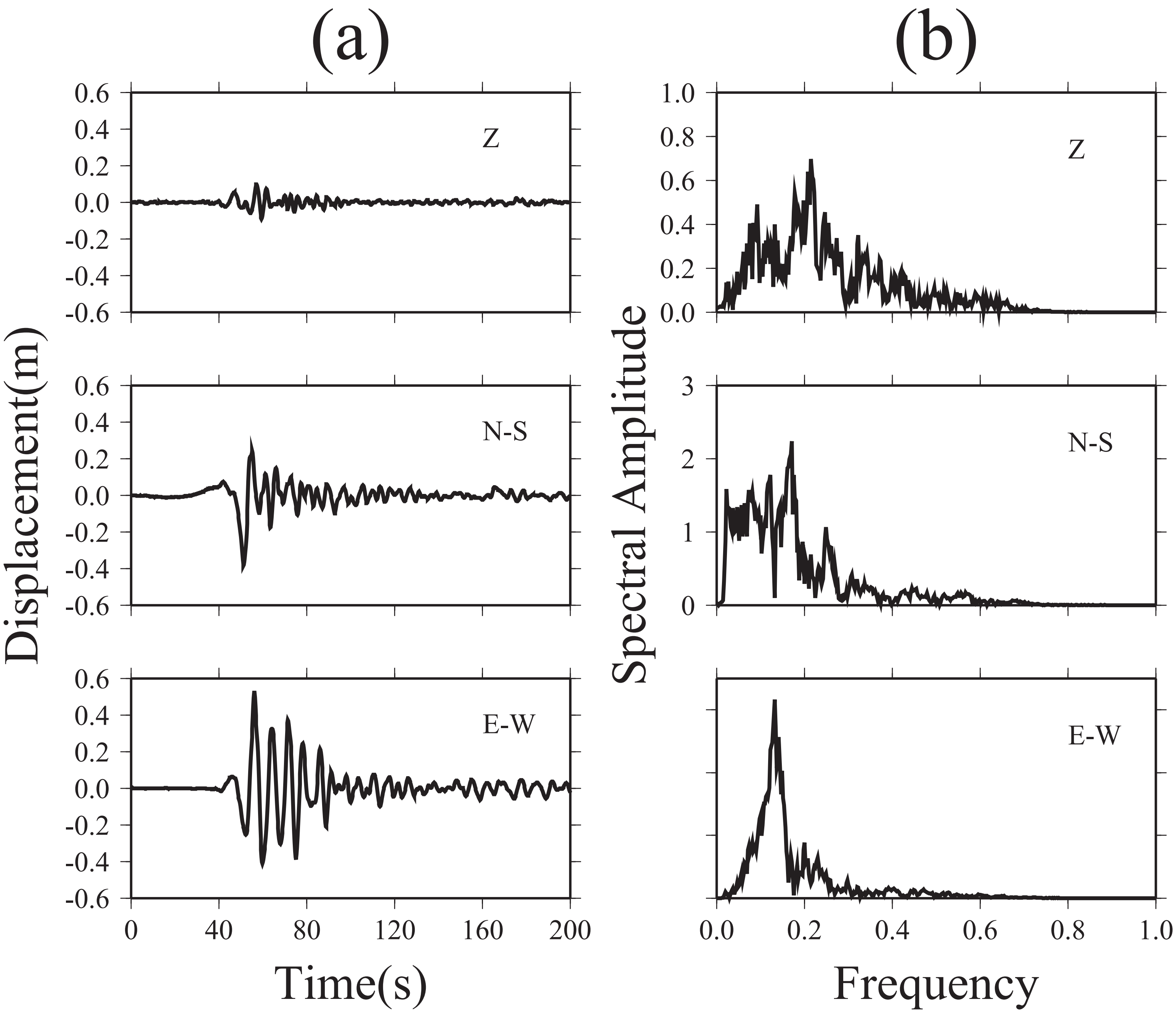
(a)
(b)
Displacement(m)
Spectral Amplitude
Z
N-S
E-W
Z
N-S
E-W
0.6
0.4
0.2
0.0
-0.2
-0.4
-0.6
1.0
0.8
0.6
0.4
0.2
0.0
3
2
1
0
0
40
80
120
160
200
0.0
0.2
0.4
0.6
0.8
1.0
Time(s)
Frequency

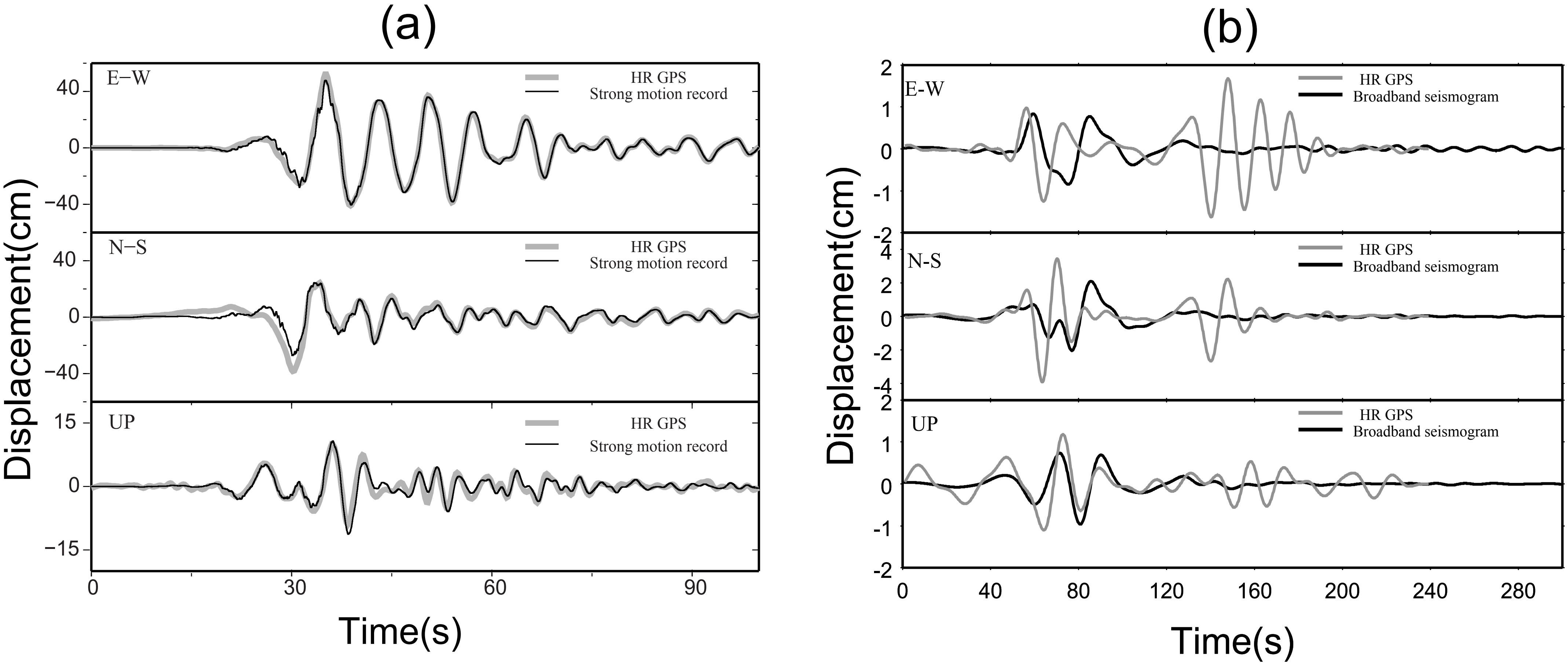

(a)
E−W
HR GPS
Strong motion record
N−S
HR GPS
Strong motion record
UP
HR GPS
Strong motion record
40
0
−40
15
−15
0
30
60
90
Displacement(cm)
Time(s)
(b)
E-W
HR GPS
Broadband seismogram
N-S
HR GPS
Broadband seismogram
UP
HR GPS
Broadband seismogram
2
1
0
-1
-2
4
-4
40
80
120
160
200
240
280
Displacement(cm)
Time(s)

Comparison of the focal mechanisms between different studies

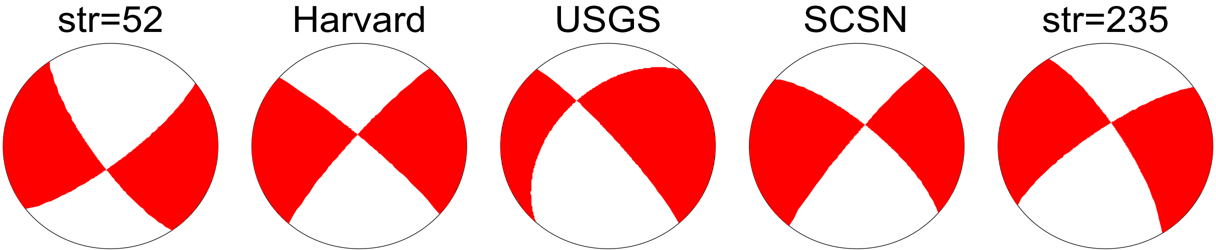

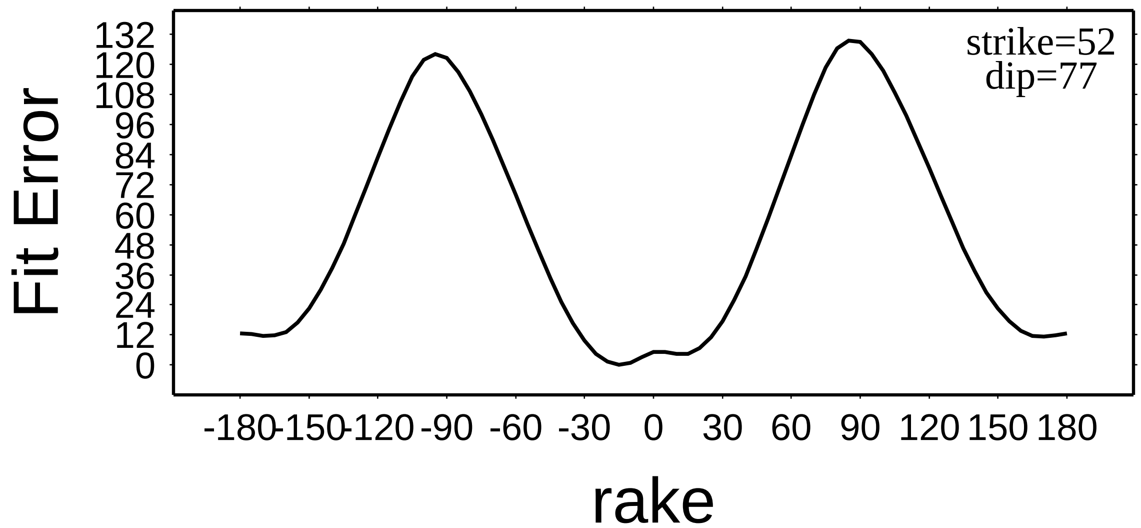
strike=52
dip=77
Fit Error
132
120
108
96
84
72
60
48
36
24
12
0
-180
-150
-120
-90
-60
-30
0
30
60
90
120
150
180
rake

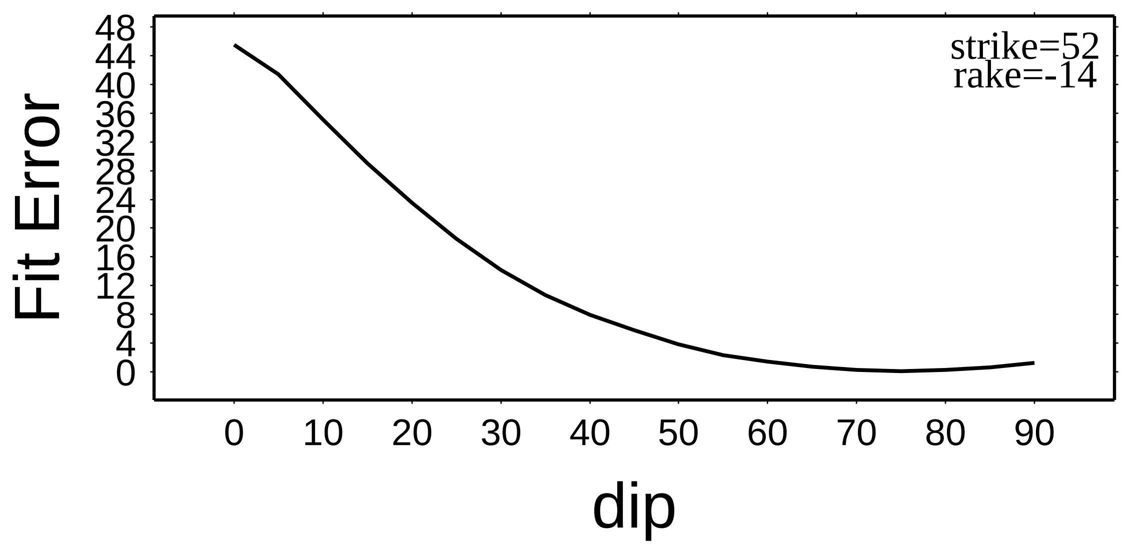
strike=52
rake=-14
Fit Error
48
44
40
36
32
28
24
20
16
12
8
4
0
0
10
20
30
40
50
60
70
80
90
dip

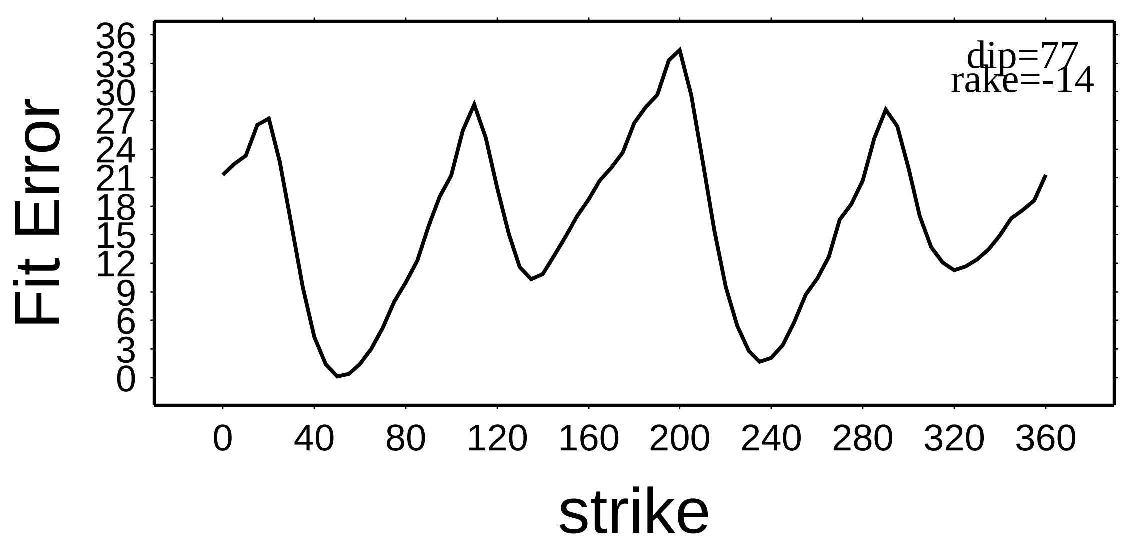
dip=77
rake=-14
Fit Error
36
33
30
27
24
21
18
15
12
9
6
3
0
0
40
80
120
160
200
240
280
320
360
strike

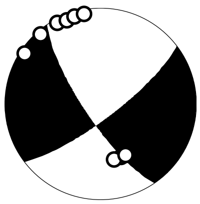

Mw 7.2 Dep: 10km
str1: 52 dip1: 77 rake1: -14
str2: 146 dip2: 76 rake2: -167